

# Enhanced Quantum Force Sensing by Digital Twinning of Atomic Bose-Einstein Condensates

Tangyou Huang<sup>1,5</sup>, Zhongcheng Yu<sup>2</sup>, Zhongyi Ni<sup>1,5</sup>, Xiaoji Zhou<sup>2,3,4</sup>,  
Xiaopeng Li<sup>5,6,1,7,8\*</sup>

<sup>1</sup>Shanghai Qi Zhi Institute, AI Tower, Xuhui District, Shanghai, 200232, China.

<sup>2</sup>State Key Laboratory of Advanced Optical Communication System and Network, School of Electronics, Peking University, Beijing 100871, China.

<sup>3</sup>Institute of Advanced Functional Materials and Devices, Shanxi University, Taiyuan 030031, China.

<sup>4</sup>Institute of carbon-based thin film electronics, Peking University, Shanxi, Taiyuan 030012, China .

<sup>5</sup>State Key Laboratory of Surface Physics, Key Laboratory of Micro and Nano Photonic Structures (MOE), and Department of Physics, Fudan University, Shanghai 200433, China.

<sup>6</sup>Institute for Nanoelectronic Devices and Quantum Computing, Fudan University, Shanghai 200433, China.

<sup>7</sup>Shanghai Artificial Intelligence Laboratory, Shanghai 200232, China.

<sup>8</sup>Shanghai Research Center for Quantum Sciences, Shanghai 201315, China.

\*Corresponding author(s). E-mail(s): [xiaopeng\\_li@fudan.edu.cn](mailto:xiaopeng_li@fudan.edu.cn);

## Abstract

High sensitivity detection plays a vital role in science discoveries and technological applications. The advancement of sensitivity has been pivotal in expanding their boundaries. While intriguing methods utilizing collective many-body correlations and quantum entanglements have been developed in physics to enhance sensitivity, their practical implementation remains challenging due to rigorous technological requirements. Here, we propose an innovative approach that harnesses the capabilities of machine learning, to significantly augment weak-signal detection sensitivity. By training a generative machine learning model on time-of-flight measurements from atomic Bose-Einstein condensates (BEC), we create a digital twinning of the experimental system, accurately matching probabilistic distributions. The digital replica is capable of generating both typical and atypical configurations, mirroring the fluctuations observed in experimental measurements caused by quantum shot-noise and technical noise. An anomaly score, quantifying the level of configuration atypicality, is obtained through the machine learning model. When an external force is applied, it perturbs the measurement outcomes of the physical system. Remarkably, even a weakly affected physical system can be detected by the machine learning model by examining the anomaly score, enabling anomaly detection. This unconventional approach to force sensing is entirely data-driven, devoid of prior knowledge about the physical system or assumptions regarding the sensing process. Our findings demonstrate a significant advancement in sensitivity, achieving an order of magnitude improvement over conventional protocols in detecting a weak force of approximately  $10^{-25}$  N. The resulting sensitivity reaches  $1.7(4) \times 10^{-25}$  N/ $\sqrt{\text{Hz}}$ . Notably, our machine learning-based signal processing approach does not rely on system-specific details or processed signals, rendering it highly applicable to sensing technologies across various domains.

# 1 Introduction

In recent decades, quantum technologies have made remarkable strides, culminating in the emergence of quantum sensing techniques that enable high-precision detection at the microscopic level. Quantum sensor leverages quantum resources to detect subtle changes in physical quantities such as time, force, and electromagnetic fields, providing extreme precision at the atomic scale [1–3]. These implementations have been successfully realized across diverse platforms, including cold atoms [4, 5], superconducting circuits [6], and solid-state spin systems [7]. Remarkably, recent progresses in quantum sensing highlight its capability for real-world applications such as precision navigation [8], gravity detection [9], dark matter searches [10] and among others [11]. However, they are often facing challenges associated with measurement uncertainty caused by quantum decoherence and back-action effects, limiting the practical applications [12, 13]. Surpassing this limit typically requires the involvement of strong correlations and high entanglement or utilizing sophisticated measurement protocols [14–17]. While hardware upgrades can enhance sensing performance, computational approaches based on signal processing and data analysis offer a somewhat more economical way to enhance the high-precision detection.

Earlier computational approaches have employed statistical learning of signal acquisition from sensing observable taking into account the inherent noise and variations [18–20]. In recent years, machine learning approaches have been used for sensing-related analysis and feature selection [9, 21, 22]. Nevertheless, these methods often demand a substantial amount of sensing data or rely on prior knowledge of signal and noise properties, thereby still limiting their applicability. More recently, the concept of digital twinning has gained significant attention as a powerful tool for simulating and understanding complex physical systems. Digital twinning involves creating a virtual replica or model that mirrors the behavior and properties of a physical system, allowing for real-time analysis, optimization, and prediction. By effectively bridging the physical and virtual realms, digital twinning provides a unique opportunity to enhance the performance and capabilities of quantum force sensing experiments.

In this article, we propose a novel application of digital twinning for quantum force sensing in atomic BECs. Leveraging the advancements in generative machine learning models, we create a digital twin that faithfully represents the atomic BEC system under investigation. The digital twin captures the intricate correlations and non-linear dynamics of the physical system, enabling us to devise a novel approach for quantum force sensing based on anomaly detection. Conventional quantum force sensing techniques often rely on extracting basic statistical moments from high-dimensional experimental data, neglecting the valuable information encoded in complex correlations. In contrast, our digital twinning approach incorporates a generative machine learning model to construct a nonlinear function, which takes advantage of the complex correlation effects in the high-dimensional data. This innovative approach allows for improved signal-to-noise ratio and enhanced sensitivity, without compromising the long-term stability of the sensing system. We anticipate that our anomaly detection technique, facilitated by digital twinning, can be broadly applied to sensing experiments involving high-dimensional data acquisition cycles. By maximizing the utilization of high-dimensional data, our approach surpasses conventional techniques that rely solely on basic statistical features, unlocking new avenues for quantum force sensing and precision measurements.

## 2 Results

**The Bose-Einstein condensate system.** We create a bosonic quantum system by trapping about  $2 \times 10^5$   $^{87}\text{Rb}$  atoms. This system forms a BEC at low temperature, about 50 nK in our experiment (Fig. 1). The atomic BEC is loaded in a triangular optical lattice to suppress unwanted real-space dynamics [23]. After preparation of the lattice BEC system, the optical lattice and the trapping potential are shut-off, which then let the atoms expand ballistically. Performing the time-of-flight (TOF) experiment, we measure the momentum distribution  $n(\mathbf{k})$ . It takes about  $T_0 = 38$  s to complete one experimental cycle.

In the time-of-flight measurements, we have shot-to-shot noise. There are quantum shot-noises, which arise from quantum superposition of different momentum eigenstates due to atomic interactions, trapping potentials, and optical lattice confinement. There are thermal noises. Although the atomic BEC is cooled down to 50 nK, we still have thermally activated atoms. These atoms induce stochastic fluctuations in the measurement outcomes. There are also technological noises. The control of the atom numbers, the trapping potential, and the optical lattice depth are not

perfect in the experiment. They may have noticeable or unnoticeable drifts in different experimental runs. As a result, the TOF measurement outcomes in the consecutive experimental runs would unavoidably fluctuate from shot to shot. We thus denote the measurement outcomes as  $n_\alpha(\mathbf{k})$ , with  $\alpha$  indexing different experimental runs.

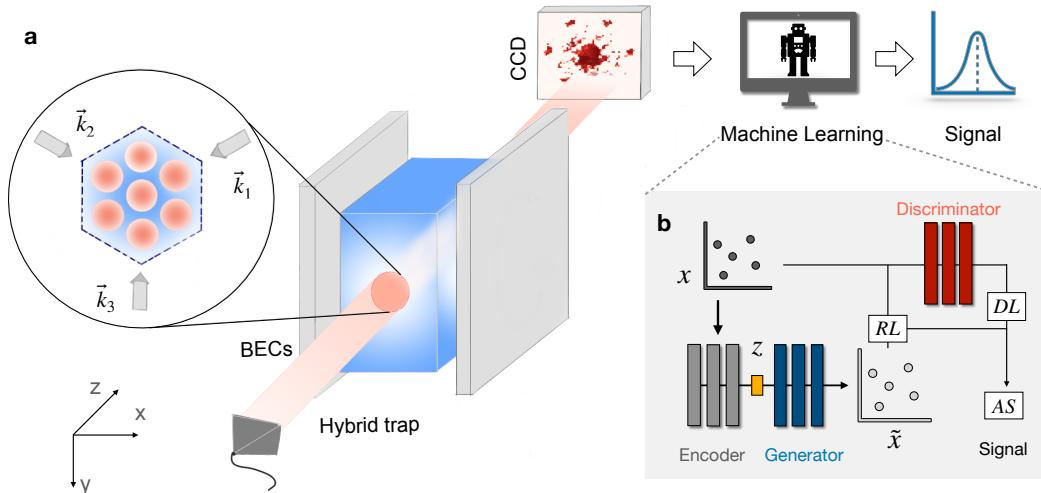


**Fig. 1** The machine-learning assisted atomic force sensing. **a.** The schematic diagram of experiment setups for an atomic BEC based force sensor. The atomic BEC is confined by a triangular optical lattice spread in the x-y plane. The time-of-flight image is probed by an imaging laser beam along the z direction, and showing on the CCD camera. With an external force applied on the BEC, the time-of-flight image would develop systematic shifts. **b.** The workflow of an *anomaly detection* method for force sensing. The generator and the discriminator form a generative machine learning model for digitally replicating the experimental time-of-flight images. The anomaly detection approach is enabled by introducing an additional encoder.

In detecting an external force acting on the BEC, a standard approach is to examine the response in the averaged center-of-mass (COM) momentum, i.e.,

$$\bar{\mathbf{k}}_{\text{COM}} = \frac{\sum_{\alpha} \int d^2\mathbf{k} n_{\alpha}(\mathbf{k}) \mathbf{k}}{\sum_{\alpha} \int d^2\mathbf{k} n_{\alpha}(\mathbf{k})}. \quad (1)$$

Although the measurement outcome  $n_{\alpha}(\mathbf{k})$  is a two-dimensional image, which potentially involves very rich information, the conventional approach of data processing following Eq. (1) only consumes the zeroth and first order moments of the two-dimensional data, leaving behind higher-order correlations.

**The digital replica.** In order to incorporate the full information in the measurement outcomes,  $n_{\alpha}(\mathbf{k})$ , one plausible way is to perform digital twinning of the physical system by matching the probability distributions. It then automatically takes into account high-order correlation effects. Since the atomic BEC system in the experiment has noises of various origins, it is impractical to simulate the experimental measurement outcomes using conventional modeling approaches, for example by simulating Gross-Pitaevskii equations [24, 25]. In this study, we create a digital twinning of the experimental system, by implementing a generative machine learning model, which incorporates quantum, thermal, and technical noise channels simultaneous at equal-footing in a purely data-driven approach.

We implement a generative adversarial network (GAN) [26] for digital twinning of the atomic BEC. GAN consists of a generator  $G(\cdot)$  that attempts to map a latent vector  $\mathbf{z}$  to a realistic data of momentum distribution,  $G(\cdot): \mathbf{z} \mapsto \tilde{n}(\mathbf{k})$ , and a discriminator  $D(\cdot)$  tries to differentiate the real data,  $n(\mathbf{k})$ , from the fake data from the generator,  $\tilde{n}(\mathbf{k}) = G(\mathbf{z})$ . The two networks are trained simultaneously, with the generator attempting to produce data that can fool the discriminator, and the discriminator learning to correctly identify synthetic data (Methods). The generator and discriminator are realized by two parameterized deep neural networks, denoted as  $G(\mathbf{z}; \theta_G)$  and  $D(n(\mathbf{k}); \theta_D)$ . We collect 3.6k independent measurements of momentum distributions, and feed to GAN. This amount of data takes about forty hours to collect in experiments, which is reasonably

affordable. In Fig. 2.a, we present fake data produced by the generator during training procedure, where the generated data is visually similar to real data, indicating that the model is capable of capturing the underlying data distribution without model collapsing. The trained generator produces a digital replica of the experimental measurements (Fig. 2.b,c), which could generate fluctuating configurations involving all noise channels automatically.

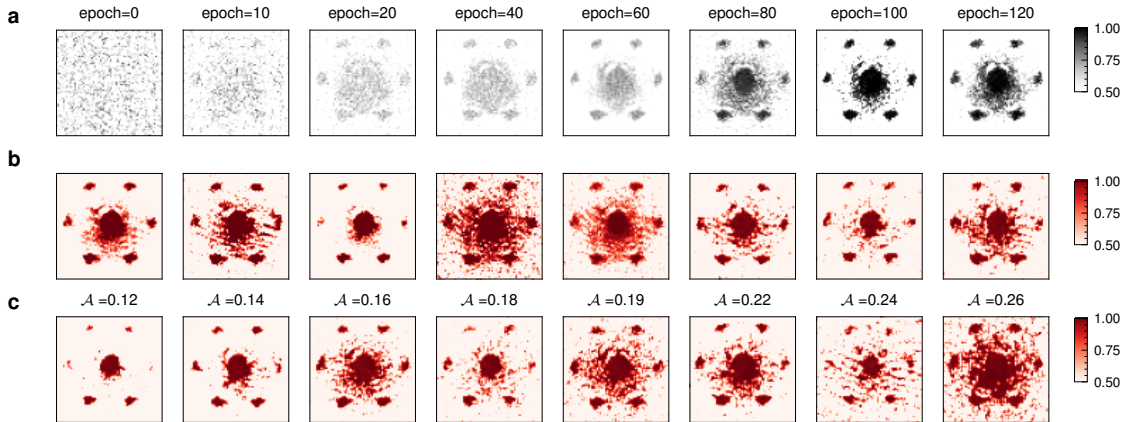


**Fig. 2 The digital replica of TOF measurements.** a. The momentum distribution constructed by generative machine learning model at different training epoch. We present several images generated from a fixed generator, namely the digital replica in b. c shows eight representative real TOF images with anomaly scores from 0.12 to 0.26.

Remarkably, even phd students cannot tell the difference between the experimental data and the data generated by the digital replica. We create two groups of data, each containing 64 TOF measurement outcomes. The first group contains real experimental data, and the second group is a mixture of real and fake data with a probability 50% : 50%. We randomly select 30 Ph.D. students and let them know how these groups are formed. They are asked to identify which ones of the second group are real experimental data. We find that the averaged accuracy is 48% [27]. This confirms the digital replica indeed captures all the features in the TOF measurements of the experimental atomic BEC.

As in the experimental data that has typical and atypical configurations due to noises, the digital replica also generates typical and atypical configurations. Within the framework of GAN, the degree of atypicality is quantified by an anomaly score,

$$\mathcal{A}(n(\mathbf{k})) = \mathcal{A}_R(n(\mathbf{k})) + \lambda \cdot \mathcal{A}_D(n(\mathbf{k})). \quad (2)$$

Here, the discrimination loss (DL)  $\mathcal{A}_D$  is directly given by the discriminator. The residual loss (RL) is produced by adding an encoder in front of the generator (Fig. 1), with  $\mathcal{A}_R = \|n(\mathbf{k}) - \tilde{n}(\mathbf{k})\|_2$ . The encoder is trained by minimizing the residual loss. The weighting coefficient  $\lambda \in \mathbb{R}$  is a hyper-parameter that balances RL and DL. These two components evaluate the discrepancy between fake and real data in terms of image distance and feature discrimination [27]. We choose  $\lambda = -0.76$  in this work. We find that the anomalous score has an approximate normal distribution (Fig. 3), which indeed reflects the typicality of momentum distribution data.

**Sensing by anomaly detection.** When an external force is applied, the physical BEC system then produces TOF data  $n(\mathbf{k})$  of different distributions. Conventional sensing schemes examine the response in the COM momentum (Eq. (1)). The distributions of the COM momentum with and without an external force are different. Force sensing requires differentiating such distributions. When a weak force ( $F_0 = 7.81 \times 10^{-26}$  N in our experiment) is applied, the distribution of COM momentum is only very weakly affected, with a barely noticeable difference from force-free distribution.

With the digital replica, namely the generative machine learning model, we compute the anomaly score  $\mathcal{A}(n(\mathbf{k}))$ , a highly nonlinear function of  $n(\mathbf{k})$ , that could incorporate higher order correlations of the data. This provides a systematic nonlinear data processing approach, much different from the linear data processing as in analyzing the simple COM momentum. Remarkably, the anomaly score is much sensitive to the force. The resultant distribution of the anomaly score caused by the weak external force is significantly different from the the force-free distribution, in sharp contrast to the COM momentum (Fig. 3). Despite the nonlinearity in the data processing, the response of the the anomaly score remains to be linear to the external force (Fig. 3.c).

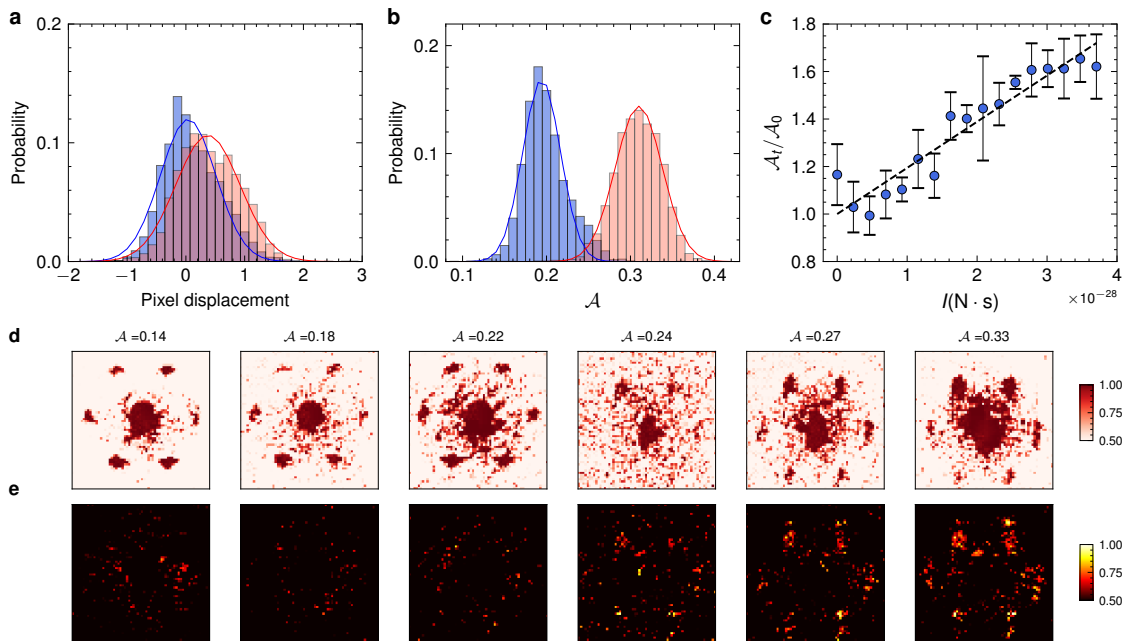


**Fig. 3 Sensing with anomaly score.** **a-b.** The probability distribution of averaged COM momentum  $\bar{\mathbf{k}}_{\text{COM}}$  (in the unit of pixels) and anomaly score  $\mathcal{A}$  in the absence of force (blue) and in the presence of force (red), respectively. Noting that the pixel displacement refers to the distance between COM and the y-axis center of pixel-wise images. **c.** The dimensionless anomaly score as a function of impulse  $I = F_0 \cdot \Delta T$  for an identical optical force  $F_0$ . The normalization factor in **c** ( $A_0$ ) is the averaged anomaly score in absence of the external force. The anomaly score  $\mathcal{A}_t(\Delta T)$  corresponds to signal-involved experiments with a force acting on the BEC for a time duration  $\Delta T$ . **d** and **e**, show the real TOF images and their corresponding anomaly localization (see the main text), respectively. Noting that the left (right) three instances in **d** are sampled from datasets with force-free (force-involved) environments.

By comparing the distributions of the COM momentum and the anomaly score, it is evident that analyzing the anomaly score, known as *anomaly detection* in the context of machine learning, is more efficient for detecting the external force applied to the BEC system.

We further investigate the primary characteristics that contribute to the anomaly score in presence of an external force. Specifically, we assess the momentum dependence of the residual loss,  $\mathcal{A}_R$ , namely,

$$n_R(\mathbf{k}) = |n(\mathbf{k}) - G^*(E^*(n(\mathbf{k})))|, \quad (3)$$

with the generator  $G^*(\cdot)$  and the encoder  $E^*(\cdot)$  being fixed. In Fig. 3.d, we provide six representative atomic images from real experimental datasets labeled with anomaly scores. In Fig. 3.e, we observe bright speckles in  $n_R(\mathbf{k})$ , with these speckles becoming increasingly prominent as the applied force intensifies. This observation suggests that the signals contributing to the anomaly scores exhibit localization in momentum space, commonly referred to as anomaly localization in the context of anomaly localization. The phenomenon of anomaly localization indicates that the machine learning model indeed captures the relevant features of the experimental data. Further discussion on model interpretability from the perspective of feature representation [28–30] is provided in Supplementary material [27]. Our findings regarding anomaly localization, exemplified by the presence of a hexagonal peak structure in the rightmost portion of Figure 3.e, imply that the dominant signal for force sensing originates primarily from high-momentum peaks observed in time-of-flight (TOF) measurements. This could be attributed to the reduced impact of various sources of noise, such as atomic scattering, trapping potential, and thermal activation, on the high-momentum components of the Bose-Einstein condensate (BEC), owing to energy separation.

**Sensitivity and Stability.** In order to quantitatively characterize the advantage of the anomaly detection over conventional approaches, we compute the corresponding sensitivity. A general force sensing process involves a force  $F$  to be detected, and a signal  $q$  that is directly or indirectly measured in the experiment. In the force sensing using the COM momentum,  $q$  corresponds to one component of  $\bar{\mathbf{k}}_{\text{COM}}$ . It corresponds to the anomaly score in the anomaly detection. The measured signals  $q$  would fluctuate in consecutive experimental measurements due to noises of various channels. We assume the induced fluctuations on  $q$  are white noise, so the fluctuations in different measurements are completely independent. The strength of the fluctuations is quantified by the standard deviation of  $q$ , to be referred to as  $\sigma_0$ . A single measurement has a fixed time cost of  $T_0$ . The minimum force we can resolve with one single-measurement is given by  $V_{\min} \sim \sigma_0/|\partial_V q|$ . Performing  $N$  times of experimental measurements, the signal to noise ratio

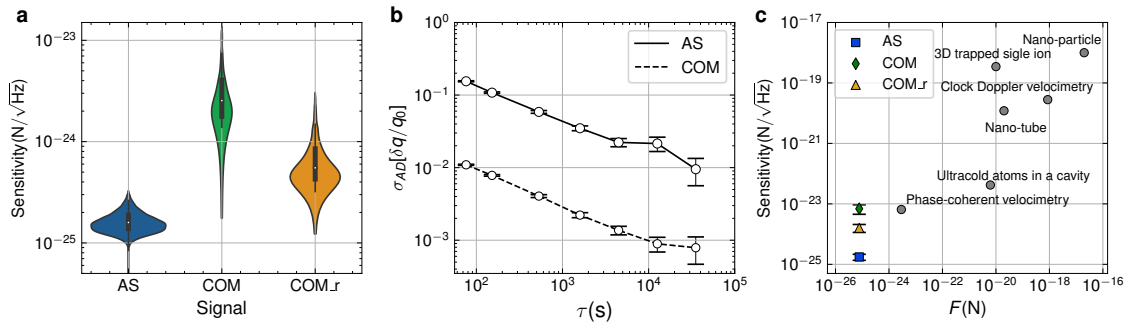


**Fig. 4 Sensitivity and stability of anomaly detection.** **a.** The sensitivity distribution of using the anomaly score (blue), COM momentum with raw data (green) and reduce datasets (yellow), respectively. In **b**, the Allan Deviations corresponding to the anomaly score and the COM momentum. Both of them decay with the integration time  $\tau$ , as  $1/\tau$ . Related works are compared in **(c)**, including measurements based on nano-tube [31], nano-particles [32], trapped ions with phase-coherent velocimetry [33], a single trapped ion with optical clock Doppler velocimetry [34], a 3D-trapped single ion [20], and ultracold atoms in a cavity [2]. Note that error bars indicate the one-sigma statistical uncertainty.

(SNR) is given by  $\text{SNR} = \sqrt{N} \times |\partial_V q V| / \sigma_0$ . The a one-sigma sensitivity is defined as [27]

$$\mathcal{S} = \sqrt{T_0} \times \frac{\sigma_0}{|\partial_V q|}. \quad (4)$$

This definition applies to both conventional approaches and the anomaly detection.

Acting linear transformation on  $q$ , the sensitivity remains the same according to Eq. (4). However, different signals that are related by nonlinear transformations do not necessarily have the same sensitivity. We compare the sensitivities of the COM momentum and the anomaly detection approaches taking exactly the same set of experimental data. For the COM momentum approach, we obtain a sensitivity  $\mathcal{S}^{\text{COM}} = 6.8(9) \times 10^{-24} \text{ N}/\sqrt{\text{Hz}}$  (Fig. 4.a). For the anomaly detection, we have  $\mathcal{S}^{\text{AS}} = 1.7(4) \times 10^{-25} \text{ N}/\sqrt{\text{Hz}}$ . This means the anomaly detection is about 40 times more sensitive than the the COM momentum approach.

We emphasize that in the above comparison we use the raw experimental data without invoking any prior knowledge of the physical process. The anomaly detection approach is thus entirely data-driven. We further examine how much the conventional COM momentum approach can be improved by machine learning based noise reduction. We perform Gaussian processing prior to extracting the COM momentum [27]. The resultant sensitivity can be improved to  $\mathcal{S}_r^{\text{COM}} = 1.6(4) \times 10^{-24} \text{ N}/\sqrt{\text{Hz}}$  (Fig. 4.a). But this is still one-order-of-magnitude worse than our anomaly detection.

In Figure 4.c, we show the comparison of the achieved sensitivity of digital twinning atomic BEC with previous experiments, including phase-coherent velocimetry [33], cold atoms in a cavity [2], and trapped ions [20]. Our achieved force sensitivity shows orders-of-magnitude improvement over other experiments. There are two remarks we would like to mention here. First, the standard quantum limit of our atomic BEC force sensor is  $5.45 \times 10^{-29} \text{ N}$  [23], which indicates there is still quite some room to improve the sensitivity here, either by improving the technical noises, or by more advanced digital twinning techniques that effectively reduces technical noises. Second, the digital twinning and the anomaly detection techniques developed here are quite generic. These techniques are readily applicable to improve the sensitivity of other experimental setups as well.

For quantum force sensing, it is also important to have long-term stability besides the high sensitivity. This is captured by the Allan Deviation [35], which is widely used to examine long-term drifts. We confirm that the Allan Deviation of the anomaly detection falls off with the integration time ( $\tau$ ) as  $1/\sqrt{\tau}$ , having the same scaling as the Allan Deviation of the COM momentum (Fig.4.b). It is thus evident that no long-term drifts are induced by the nonlinear data processing in anomaly detection. The  $1/\sqrt{\tau}$  decay also implies the fluctuations of the anomaly score are mainly white noise, which justifies the above definition of sensitivity.

It is worth noting here that the sensitivity can also be enhanced by choosing the high data-quality region of the TOF measurements according to the impulse theorem, as used in a previous study [23]. Such analysis requires certain prior information of the force, and gives a sensitivity comparable to the present anomaly detection approach. Nonetheless, we emphasize that the anomaly detection approach is purely data driven, and is consequently more robust against long-term drifts in experiments. The improvement in the long-term stability is evident by comparing the Allan Deviation of the anomaly detection to the pervious study [23]. In the previous study,

the Allan Deviation bends up at a time scale of  $\tau = 10^4$  s, whereas it keep decreasing following  $1/\sqrt{\tau}$  even at the time scale of  $4 \times 10^4$  s.

### 3 Discussion

In this study, we present a novel method for quantum force sensing using digital twinning of atomic BEC and anomaly detection facilitated by a generative machine learning model. By incorporating complex correlation effects present in the experimental data through nonlinear processing, we achieve a significant enhancement in sensitivity while maintaining long-term stability. Unlike conventional approaches that rely on extracting basic statistical moments from high-dimensional data, such as time-of-flight (TOF) measurements in BEC, our anomaly detection approach employs a neural network-based nonlinear function, denoted as  $f_{\text{NN}}(\mathbf{x})$ , to fully exploit the information within the high-dimensional data. Through extensive training and iterative refinement, this methodology effectively amplifies the signal-to-noise ratio, as confirmed by convergence in sensitivity with increasing training data [27].

Notably, our findings reveal an intriguing aspect: the sensitivity of a physical sensor is intimately tied to the data processing strategy, denoted as  $\mathcal{S}[f_{\text{NN}}]$ . This implies the existence of an upper bound,

$$\mathcal{S}_{\text{opt}} = \max_{f_{\text{NN}}} \{\mathcal{S}[f_{\text{NN}}]\}, \quad (5)$$

which represents the maximum achievable sensitivity attainable by a given sensor configuration. The determination of this upper bound warrants further investigation in future research endeavors.

The other important direction is to investigate the fundamental quantum limits of the anomaly detection approach. How the optimal sensitivity  $\mathcal{S}_{\text{opt}}$  is fundamentally limited by the quantum shot-noise, and its scaling with the number of atoms in the BEC or the imaging resolution, are worth further theoretical studies.

**Acknowledgments.** We acknowledge helpful discussion with W. Vincent Liu. This work is supported by National Program on Key Basic Research Project of China (Grant No. 2021YFA1400900), National Natural Science Foundation of China (Grants No. 11934002, 12075128, T2225008), Shanghai Municipal Science and Technology Major Project (Grant No. 2019SHZDZX01), and Shanghai Science Foundation (Grants No.21QA1400500).

## 4 Methods

### Generative Adversarial Networks

Generative Adversarial Networks (GANs) are a class of deep learning models used for unsupervised learning tasks, such as artificial image generation and information processing [26]. Our goal is to utilize GANs as the generative model to construct the digital replica of our experimental data. We start with a set of raw observable  $X = \{\mathbf{x}_1, \mathbf{x}_2, \mathbf{x}_3, \dots, \mathbf{x}_N\}$  measured from  $N$  independent experiments. Next, we shall train the GAN relying on finite number of datasets  $X$ . Generally, a GAN consists of a *generator*  $G(\cdot)$  that mapping the latent vector  $\mathbf{z}$  to a realistic data  $G(\cdot): \mathbf{z} \mapsto \tilde{\mathbf{x}}$ , and a *discriminator*  $D(\cdot)$  identifies the real  $\mathbf{x} \in X$  rather than the fake data  $\tilde{\mathbf{x}} = G(\mathbf{z})$  from the generator. The two networks are trained simultaneously, with the generator attempting to produce data that can fool the discriminator, and the discriminator learning to correctly identify synthetic data. In general, the generator and discriminator are realized by two parameterized deep neural networks, i.e.,  $G(\mathbf{z}; \theta_G)$  and  $D(\mathbf{x}; \theta_D)$ . In this sense, parameter  $\theta_D, \theta_G$  are simultaneously optimized for a standard min-max loss function  $V(D, G)$  [36]:

$$\min_G \max_D V(D, G) = \mathbb{E}_{\mathbf{x} \sim \mathcal{P}_0} [\log D(\mathbf{x})] + \mathbb{E}_{\mathbf{z} \sim \mathcal{P}_z} [\log(1 - D(G(\mathbf{z})))] \quad (6)$$

$\theta_D$  and  $\theta_G$  are respectively adjusted to maximize the expectation value  $\mathbb{E}_{\mathbf{x} \sim \mathcal{P}_0}$  and minimize the  $\mathbb{E}_{\mathbf{z} \sim \mathcal{P}_z}$ . GANs work by training a generator network to produce synthetic data that resembles the healthy distribution  $\mathbf{x} \sim \mathcal{P}_0(\mathbf{x})$ , while a discriminator network is trained to distinguish the data out of healthy distribution. In this vein, the convergence criteria is that the generator is able to fool the discriminator, resulting in the high-quality digital replica of training data.

### Anomaly detection

GANs are widely used in anomaly detection due to their ability to learn complex data distributions, making them effective in identifying anomalies that deviate from the healthy distribution. Hereby,

an anomaly is to quantify the similarity of query data from the health distribution  $\mathcal{P}_0(\mathbf{x})$ . To identify anomalies via the GAN model, the authors in [28] proposed a *AnoGAN* structure to detect the degree of anomaly quantitatively. More specifically, for a query data  $\mathbf{x}$ : first, one shall find the optimal representation  $\mathbf{z}_\gamma$  from the latent space  $\mathcal{Z}$  to guarantee the maximum degree of similarity between original data  $\mathbf{x}$  and generated data  $\tilde{\mathbf{x}} = G(\mathbf{z}_\gamma)$ , and computing the *residual loss* (RL); second, calculating the *discrimination loss* (DL) from the perspective of feature layers; third, the overall loss as the weighted sum of RL and DL resulted as anomaly score (AS). For this purpose, we define the RL  $\mathcal{A}_R(\mathbf{x}) = \frac{1}{n_x} \sum |\mathbf{x} - G^*(\mathbf{z}_\gamma)|$ , and the DL  $\mathcal{A}_D(\mathbf{x}) = \frac{1}{n_f} \sum |h(\mathbf{x}) - h(G^*(\mathbf{z}_\gamma))|$ , where  $h(\cdot)$  refers to the feature layer of an intermediate layer of the discriminator and  $n_x, n_f$  corresponding pixel numbers. Therefore, the anomaly score is defined as in Eq. (2), e.g.,  $\mathcal{A}(\mathbf{x}) = \mathcal{A}_R(\mathbf{x}) + \lambda \cdot \mathcal{A}_D(\mathbf{x})$ , where the hyperparameter  $\lambda$  is a weighted coefficient. Note that the generator  $G^*(\theta_G^*)$  and discriminator  $D^*(\theta_D^*)$  are fixed from the previous adversarial training, and only the input vector  $\mathbf{z}$  is adapted via backpropagation for a query data  $\mathbf{x}$  [28]. Remarkably, a higher precise generator can be realized by introducing the inverse mapping  $\mu(\tilde{\mathbf{x}}) \rightarrow \mathbf{z}$ . Instead of direct backpropagation [28], we here apply an adaptive method [29] called *f-AnoGAN* by introducing the extra DNN *encoder*  $E(\cdot)$  which can be trained only on  $X$  to automatically produce latent vector for any inputting data, e.g.,  $\mathbf{z}_\gamma = E(\mathbf{x})$ , see details in supplementary material [27]. Accordingly, the anomaly detection via *f-AnoGAN* is concluded as follows: the GAN should be initially trained on the datasets  $X$  (signal-free) sampled from the healthy distribution  $\mathcal{P}_0(\mathbf{x})$ , and the anomaly detection is subsequently processing by evaluating the anomaly score  $\mathcal{A}(\mathbf{x})$  (Eq. (2)) for arbitrary data  $\mathbf{x} \in \mathcal{X}$ . The model yields large AS for data from a destructive distribution  $\mathcal{P}(\mathbf{x})$ , whereas a small AS refers to the high probability of query data from the health distribution  $\mathcal{P}_0(\mathbf{x})$ . We refer the reader to supplement materials [27] for details about model training and evaluation.

As a result, we obtain a fixed GAN-based generative model to automatically output the anomaly score  $\mathcal{A} = f_{\text{NN}}^*(\mathbf{x}|\{\theta_G^*, \theta_D^*\})$  for data  $\mathbf{x} \in \mathcal{X}$ . In a sensing application, the anomaly score assigned for signal-free experimental outcomes follows the healthy probability distribution  $\mathbb{P}_0(\mathcal{A}(\mathbf{x}))$ . When it comes to an unknown perturbation  $V$  (i.e., an external force in our setup), a destructive probability distribution  $\tilde{\mathbb{P}}(\mathcal{A}(\tilde{\mathbf{x}}))$  as well can be formed according to our fixed model, see the workflow in Fig.1. The former anomaly score of signal-free are statistically smaller than the later one, indicating that sensitive signal (anomaly score) could be formulated by anomaly detection method.

## DATA AVAILABILITY

Data are available from the authors upon reasonable request.

## CODE AVAILABILITY

The computation code for producing the results in this work is available upon reasonable request.

## AUTHOR CONTRIBUTION

X.L. conceived the main idea in discussion with T.H. and X.J.Z. T.H. designed the machine learning framework and carried out the tests. Z.C.Y. contributed to the experimental data analysis. All authors contributed to writing the paper.

## COMPETING INTERESTS

The authors declare no competing interests.

## References

- [1] Huntemann, N., Sanner, C., Lipphardt, B., Tamm, C. & Peik, E. Single-ion atomic clock with  $3 \times 10^{-18}$  systematic uncertainty. *Phys. Rev. Lett.* **116**, 063001 (2016). URL <https://link.aps.org/doi/10.1103/PhysRevLett.116.063001>.
- [2] Schreppler, S. *et al.* Optically measuring force near the standard quantum limit. *Science* **344**, 1486–1489 (2014). URL <https://www.science.org/doi/abs/10.1126/science.1249850>.
- [3] Wang, G. *et al.* Sensing of arbitrary-frequency fields using a quantum mixer. *Phys. Rev. X* **12**, 021061 (2022). URL <https://link.aps.org/doi/10.1103/PhysRevX.12.021061>.
- [4] Facon, A. *et al.* A sensitive electrometer based on a rydberg atom in a schrödinger-cat state. *Nature* **535**, 262–265 (2016). URL <https://www.nature.com/articles/nature18327>.

- [5] Szigeti, S. S., Nolan, S. P., Close, J. D. & Haine, S. A. High-precision quantum-enhanced gravimetry with a bose-einstein condensate. *Phys. Rev. Lett.* **125**, 100402 (2020). URL <https://link.aps.org/doi/10.1103/PhysRevLett.125.100402>.
- [6] Halbertal, D. *et al.* Nanoscale thermal imaging of dissipation in quantum systems. *Nature* **539**, 407–410 (2016). URL <https://www.nature.com/articles/nature19843>.
- [7] Taylor, J. M. *et al.* High-sensitivity diamond magnetometer with nanoscale resolution. *Nature Physics* **4**, 810–816 (2008). URL <https://www.nature.com/articles/nphys1075>.
- [8] Bidel, Y. *et al.* Absolute marine gravimetry with matter-wave interferometry. *Nature communications* **9**, 627 (2018). URL <https://www.nature.com/articles/s41467-018-03040-2>.
- [9] Stray, B. *et al.* Quantum sensing for gravity cartography. *Nature* **602**, 590–594 (2022). URL <https://www.nature.com/articles/nphys4074>.
- [10] Arvanitaki, A., Graham, P. W., Hogan, J. M., Rajendran, S. & Van Tilburg, K. Search for light scalar dark matter with atomic gravitational wave detectors. *Phys. Rev. D* **97**, 075020 (2018). URL <https://link.aps.org/doi/10.1103/PhysRevD.97.075020>.
- [11] Bongs, K. *et al.* Taking atom interferometric quantum sensors from the laboratory to real-world applications. *Nature Reviews Physics* **1**, 731–739 (2019). URL <https://www.nature.com/articles/s42254-019-0117-4>.
- [12] Braginsky, V. B. & Khalili, F. Y. Quantum nondemolition measurements: the route from toys to tools. *Rev. Mod. Phys.* **68**, 1–11 (1996). URL <https://link.aps.org/doi/10.1103/RevModPhys.68.1>.
- [13] Braginsky, V. B., Braginskii, V. B. & Khalili, F. Y. *Quantum measurement* (Cambridge University Press, 1995).
- [14] Mason, D., Chen, J., Rossi, M., Tsaturyan, Y. & Schliesser, A. Continuous force and displacement measurement below the standard quantum limit. *Nature Physics* **15**, 745–749 (2019). URL <https://www.nature.com/articles/s41567-019-0533-5>.
- [15] Kampel, N. S. *et al.* Improving broadband displacement detection with quantum correlations. *Phys. Rev. X* **7**, 021008 (2017). URL <https://link.aps.org/doi/10.1103/PhysRevX.7.021008>.
- [16] Yu, H. *et al.* Quantum correlations between light and the kilogram-mass mirrors of ligo. *Nature* **583**, 43–47 (2020). URL <https://www.nature.com/articles/s41586-020-2420-8>.
- [17] Tanaka, T. *et al.* Proposed robust entanglement-based magnetic field sensor beyond the standard quantum limit. *Phys. Rev. Lett.* **115**, 170801 (2015). URL <https://link.aps.org/doi/10.1103/PhysRevLett.115.170801>.
- [18] Pertsinidis, A., Zhang, Y. & Chu, S. Subnanometre single-molecule localization, registration and distance measurements. *Nature* **466**, 647–651 (2010). URL <https://www.nature.com/articles/nature09163>.
- [19] Grote, H., Schnabel, R. & Vahlbruch, H. A gravitational wave observatory operating beyond the quantum shot-noise limit. *Nature Physics* **7**, 962–965 (2011). URL <https://www.nature.com/articles/nphys2083>.
- [20] Blüms, V. *et al.* A single-atom 3d sub-attoneutron force sensor. *Science advances* **4**, eaao4453 (2018). URL <https://www.science.org/doi/full/10.1126/sciadv.aao4453>.
- [21] Cho, S.-Y. *et al.* Finding hidden signals in chemical sensors using deep learning. *Analytical chemistry* **92**, 6529–6537 (2020). URL <https://pubs.acs.org/doi/10.1021/acs.analchem.0c00137>.
- [22] Colgan, R. E. *et al.* Efficient gravitational-wave glitch identification from environmental data through machine learning. *Phys. Rev. D* **101**, 102003 (2020). URL <https://link.aps.org/doi/10.1103/PhysRevD.101.102003>.

- [23] Guo, X. *et al.* Quantum precision measurement of two-dimensional forces with 10-28-newton stability. *Science Bulletin* **67**, 2291–2297 (2022). URL <https://www.sciencedirect.com/science/article/pii/S2095927322004881>.
- [24] Gross, E. P. Structure of a quantized vortex in boson systems. *Il Nuovo Cimento (1955-1965)* **20**, 454–477 (1961). URL <https://doi.org/10.1007/BF02731494>.
- [25] Pitaevskii, L. P. Vortex lines in an imperfect bose gas. *Sov. Phys. JETP* **13**, 451–454 (1961).
- [26] Goodfellow, I., Bengio, Y. & Courville, A. *Deep Learning* (MIT Press, 2016). URL <http://www.deeplearningbook.org>.
- [27] Huang, T., Zhongcheng, Y., Zhongyi, N., Xiaoji, Z. & Xiaopeng, L. Supplementary material. *Supplementary material on the details of "Enhanced Quantum Force Sensing by Digital Twinning of Atomic Bose-Einstein Condensates"* URL [xxxx](#).
- [28] Schlegl, T., Seeböck, P., Waldstein, S. M., Schmidt-Erfurth, U. & Langs, G. Unsupervised anomaly detection with generative adversarial networks to guide marker discovery. *International conference on information processing in medical imaging* 146 (2017). URL [https://link.springer.com/chapter/10.1007/978-3-319-59050-9\\_12](https://link.springer.com/chapter/10.1007/978-3-319-59050-9_12).
- [29] Schlegl, T., Seeböck, P., Waldstein, S. M., Langs, G. & Schmidt-Erfurth, U. fanogan: Fast unsupervised anomaly detection with generative adversarial networks. *Medical image analysis* **54**, 30–44 (2019). URL <https://www.sciencedirect.com/science/article/abs/pii/S1361841518302640>.
- [30] Huang, T., Ban, Y., Sherman, E. Y. & Chen, X. Machine-learning-assisted quantum control in a random environment. *Phys. Rev. Appl.* **17**, 024040 (2022). URL <https://link.aps.org/doi/10.1103/PhysRevApplied.17.024040>.
- [31] Moser, J. *et al.* Ultrasensitive force detection with a nanotube mechanical resonator. *Nature nanotechnology* **8**, 493–496 (2013). URL <https://www.nature.com/articles/nmano.2013.97>.
- [32] Hebestreit, E., Frimner, M., Reimann, R. & Novotny, L. Sensing static forces with free-falling nanoparticles. *Phys. Rev. Lett.* **121**, 063602 (2018). URL <https://link.aps.org/doi/10.1103/PhysRevLett.121.063602>.
- [33] Biercuk, M. J., Uys, H., Britton, J. W., VanDevender, A. P. & Bollinger, J. J. Ultrasensitive detection of force and displacement using trapped ions. *Nature nanotechnology* **5**, 646–650 (2010). URL <https://www.nature.com/articles/nmano.2010.165>.
- [34] Shaniv, R. & Ozeri, R. Quantum lock-in force sensing using optical clock doppler velocimetry. *Nature communications* **8**, 14157 (2017). URL <https://www.nature.com/articles/ncomms14157>.
- [35] Leeson, D. B. A simple model of feedback oscillator noise spectrum. *Proceedings of the IEEE* **54**, 329–330 (1966). URL <https://ieeexplore.ieee.org/abstract/document/1446612/>.
- [36] Goodfellow, I. *et al.* Generative adversarial nets **27** (2014). URL <https://proceedings.neurips.cc/paper/2014/file/5ca3e9b122f61f8f06494c97b1afccf3-Paper.pdf>.
- [37] Degen, C. L., Reinhard, F. & Cappellaro, P. Quantum sensing. *Rev. Mod. Phys.* **89**, 035002 (2017). URL <https://link.aps.org/doi/10.1103/RevModPhys.89.035002>.
- [38] Cywiński, L., Lutchny, R. M., Nave, C. P. & Das Sarma, S. How to enhance dephasing time in superconducting qubits. *Phys. Rev. B* **77**, 174509 (2008). URL <https://link.aps.org/doi/10.1103/PhysRevB.77.174509>.
- [39] Medford, J. *et al.* Scaling of dynamical decoupling for spin qubits. *Phys. Rev. Lett.* **108**, 086802 (2012). URL <https://link.aps.org/doi/10.1103/PhysRevLett.108.086802>.
- [40] Barry, J. F. *et al.* Sensitivity optimization for nv-diamond magnetometry. *Rev. Mod. Phys.* **92**, 015004 (2020). URL <https://link.aps.org/doi/10.1103/RevModPhys.92.015004>.

- [41] Goodfellow, I. *et al.* Generative adversarial networks. *Communications of the ACM* **63**, 139–144 (2020). URL <https://dl.acm.org/doi/abs/10.1145/3422622>.
- [42] Arjovsky, M., Chintala, S. & Bottou, L. *Wasserstein generative adversarial networks*, 214–223 (PMLR, 2017). URL <https://proceedings.mlr.press/v70/arjovsky17a>.
- [43] Kingma, D. P. & Ba, J. Adam: A method for stochastic optimization. *arXiv preprint arXiv:1412.6980* (2014). URL <https://arxiv.org/abs/1412.6980>.
- [44] Group, G. R. *A data analysis and machine learning tool* URL <https://colab.research.google.com/>.
- [45] Van der Maaten, L. & Hinton, G. Visualizing data using t-sne. *Journal of machine learning research* **9** (2008). URL <https://www.jmlr.org/papers/volume9/vandermaaten08a/vandermaaten08a.pdf?fbcl>.
- [46] Streed, E. W., Jechow, A., Norton, B. G. & Kielpinski, D. Absorption imaging of a single atom. *Nature communications* **3**, 933 (2012). URL <https://www.nature.com/articles/ncomms1944>.

# Supplementary Material

## S-1 Derivation of the sensitivity

We start with two probability distributions of signal  $q$  for  $N$  independent sensing experiments, i.e.,  $\mathbb{P}_0(q)$  and  $\mathbb{P}_\delta(q)$ , which refer to the healthy and destructive distribution, respectively. In other words, the signal initially obeys  $q \sim \mathbb{P}_0(q)$  with static quantity  $V_0$ , and follows an destructive distribution  $q \sim \mathbb{P}_\delta(q)$  after interacting with  $V = V_0 + \delta V$ . The readout error occurs when determining whether a query signal  $q$  belongs to  $\mathbb{P}_\delta$  instead of  $\mathbb{P}_0$ , which can be quantified as the variance  $\sigma^2 = 1/(4C^2N)$  [37] with efficiency coefficient  $C \in [0, 1]$ . Where  $C = 1$  indicates the experiment observable can be perfectly identified, and  $C = 0$  refers to the sensor is not able to detect the signal in a finite number of experiments. It's worth to note that  $C = 1/4$  refers the statistic signal  $q$  belong to a the Gaussian distribution in this case. On the other hand, we consider the decoherence effect resulting as the exponentially decay on the signal change  $\delta q(t) = \delta q e^{-\chi(t)}$  during the sensing period  $t \in [0, T]$ , where  $q_0 = q(0)$  and the  $\chi(t)$  is an empirical function that depends on the decoherence of quantum resource [38, 39]. Note that we define the partial derivative of signal fluctuation  $\partial_V q = \delta q / \delta V$  respect to a small change of physical quantity  $\delta V$ . As a result, we obtain the signal-to-noise as

$$\text{SNR} = \frac{\delta q e^{-\chi(t)}}{\sigma} = 2\delta V |\partial_V q| e^{-\chi(t)} C \sqrt{N}, \quad (\text{S1})$$

where the experiment count  $N$  can be represented in a time basis as  $N = T/(t + t_m)$ , where  $T$ ,  $t$  and  $t_m$  are the total time, sensing time and the time for sensor initialization and measurement of single experiment, respectively. Generally, the signal change  $\delta q$  is a function of quantity  $\delta V$  i.e.,  $\delta q \propto (\delta V)^k$  with  $k = 1, 2$  for a Ramsey experiment [40]. The minimum detectable physical quantity  $V_{\min}$  is resulted from unit SNR respect to the measurement uncertainty, e.g.,  $\delta q = \sigma$ . In this vein, the *sensitivity* is interpreted the minimum detectable signal that yields unit SNR over one second ( $T = 1s$ ) [37]

$$\text{sensitivity} := \frac{e^{\chi(t)} \sqrt{t + t_m}}{2C |\partial_V^k q|}. \quad (\text{S2})$$

The above equation provides a general expression for the definition of *sensitivity* in quantum sensing applications. In our case, we assume the signal respond  $\delta q$  is a linear function of perturbation  $\delta V$  since  $\delta V \rightarrow 0$  in high-precision detection. Meanwhile, we suppose the single experiment time  $T_0$  is smaller than the coherence time for avoiding the exponential decoherence effect. Without loss of generality, we define the minimum detectable quantity is resulted at one-sigma uncertainty of health distribution  $\sigma_0 = \sqrt{\text{var}[\mathbb{P}_0(q)]}$ , leading to the *sensitivity* definition:

$$\mathcal{S} = \sqrt{T_0} \times \frac{\sigma_0}{|\partial_V q|}, \quad (\text{S3})$$

where  $T_0 = t + t_m$  is the time cost for single experiment. Since the noise interference is usually inevitable on a pre-tolerance quantum device, one can reduce the readout noise by performing a large number of experiments  $N \rightarrow +\infty$ . However, it is prohibited in a state-of-the-art quantum experiment due to the decoherence effect. In this regard, our method aims to optimize the signal construction  $f(\cdot) : V \mapsto q$  for increasing the sensitivity.

## S-2 The unsupervised learning of the *f-AnoGAN*

In this section, we introduce the training procedure including the model structure and loss functions, where the source data and codes are available from the corresponding author upon request. In our setup, we collect  $3.6 \times 10^3$  two-dimension (2D) TOF atomic images with and without in the present of optical-force. The training datasets  $X$  contains 90% of total experimental outcome, and the rest as testing datasets. Each images are converted to the resolution  $64 \times 64$ , and normalized to range  $\mathbf{x} \in [-1, 1]^n$ .

The discriminator  $D(\theta_D)$  is a binary classifier to classify the real data  $\mathbf{x} \sim \mathcal{P}_{\text{data}}$  and reconstructed data  $\tilde{\mathbf{x}} \sim \mathcal{P}_g$ , where the output contain one-dimension scalar  $p_D \in [0, 1]$  representing the probability of being a real data for a inputting query image. Noting that the hidden layers of discriminator consists a few perception layers before the activation layer. And we choose the

last layer of discriminator as our feature layer  $h(\mathbf{x})$ . The generator  $G(\theta_G)$  is composed by multiply fully-connected artificial neural works, where its input is a latent vector  $\mathbf{z}$  with dimensionality 100 randomly drawn from a uniform distribution  $\mathbf{z} \sim \mathcal{P}_z \in \mathbb{R}$  and the output  $\tilde{\mathbf{x}}$  is a reconstructed image with the same resolution size.

In the frame of GANs, the goal of discriminator is accurately classifying the real data  $\mathbf{x}$  as real and the generated data  $\tilde{\mathbf{x}}$  false. For a minibatch  $m$  samples, the training process of the discriminator focuses on updating and maximizing:

$$L_D = \frac{1}{m} \sum_{i=1}^m [\log D(\mathbf{x}^{(i)}) + \log(1 - D(G(\mathbf{z}^{(i)})))] . \quad (S4)$$

The *generator* aims to fool the *discriminator* by minimizing the loss function

$$L_G = \frac{1}{m} \sum_{i=1}^m (1 - D(G(\mathbf{z}))) . \quad (S5)$$

In other words,  $D$  and  $G$  are trained with the minimax loss function:

$$\min_G \max_D V(D, G) = \mathbb{E}_{\mathbf{x} \sim \mathcal{P}_{data}} [\log D(\mathbf{x})] + \mathbb{E}_{\mathbf{z} \sim \mathcal{P}_z} [\log(1 - D(G(\mathbf{z})))] . \quad (S6)$$

where trainable parameters  $\{\theta_D, \theta_G\}$  are sequentially optimized in a generative adversarial training process. The above training process theoretically provides the convergence condition at  $\mathcal{P}_{data} = \mathcal{P}_g$  resulting the minimum loss value 0 for  $D$  and  $-\log 4$  [41] for  $G$ . In the early stage of training the GAN [28, 36], the loss function Eq.(S5 – S4) are designed to minimize the Jensen-Shannon (JS) divergence between the distribution of realistic data  $\mathcal{P}_{data}$  and generated images from the generator  $\mathcal{P}_g$ . However, this formulation usually suffers from gradient collapse, and it leads to the failure of training a GAN. Remarkably, *Arjovsky et al* [42] proposed to use the Wasserstein distance instead of JS divergence since it provide a smoother training landscape. In our case, we apply the Wasserstein distance to train our GAN, e.g., using a Wasserstein GAN (WGAN)[42]. To formulate the *anomaly detection*, we shall find the best  $\mathbf{z}_\gamma \in \mathcal{Z}$  and fed it into the trained generator  $G^*(\mathbf{z}_\gamma)$  to obtain the maximum similarity between reconstructed data and real data. In the original paper [28], they optimize the coefficient  $\mathbf{z}$  (via an auto propagation optimization process) to minimize the distance between real and fake images, aiming to find the optimized  $\mathbf{z} = \mathbf{z}_\gamma$  for achieving the most similar image  $G^*(\mathbf{z}_\gamma)$  with  $x$ . This method has drawback that it lacks the flexibility on real world applications. To acquire an adaptive latent coefficient  $\mathbf{z} \in \mathcal{Z}$ , we implement an *encoder*  $E(x)$  network to train the reverse mapping  $E(\mathbf{x}) \rightarrow \mathbf{z}$ , where the input  $\mathbf{x} \in X$  and output latent vector  $\mathbf{z}$ . The training database is the same as we used in WGAN training process, and we apply the *izif*-typed loss function [29]

$$L_E(x) = \frac{1}{n_x} \sum_{i=1}^{n_x} |x - G^*(E(x))|^2 + \frac{\lambda}{n_f} \sum_{i=1}^{n_f} |h(x) - h(G^*(E(x)))|^2, \quad (S7)$$

where  $n_x$  and  $n_f$  are the pixel number in an image  $\mathbf{x}$  and the corresponding feature map  $h(\mathbf{x})$  of the fixed discriminator  $D^*(\mathbf{x})$  and the weighted constant  $\lambda$ . This method using a extra network called *encoder* to map the latent in anomaly detection is called fast *AnoGAN* (*f-AnoGAN*), see more detail in Ref [29]. Meanwhile, we use the symbol  $E^*(\cdot)$  represents the fixed *encoder* after training on datasets  $X$ . To this end, we have the fixed GAN combining of discriminator  $D^*(\mathbf{x})$ , generator  $G^*(\mathbf{x})$  and encoder  $E^*(\mathbf{x})$ . Here, we apply a stochastic gradient-descent based optimizer **Adam**() [43] for mentioned optimization training processes. And the whole data processing and training algorithm are performed in the **Pytorch** platform with GPU acceleration using computation resource in cloud service **Colaboratory** [44].

*The anomaly score.* According to the fixed networks  $G^*(\cdot)$ ,  $D^*(\cdot)$  and  $E^*(\cdot)$ , we then calculate the anomaly score defined by the Eq.(2) in the main context. First, the *residual loss* (RL) score is directly calculated by

$$\mathcal{A}_R(\mathbf{x}) = \frac{1}{n_x} \sum |\mathbf{x} - G^*(E^*(\mathbf{x}))|. \quad (S8)$$

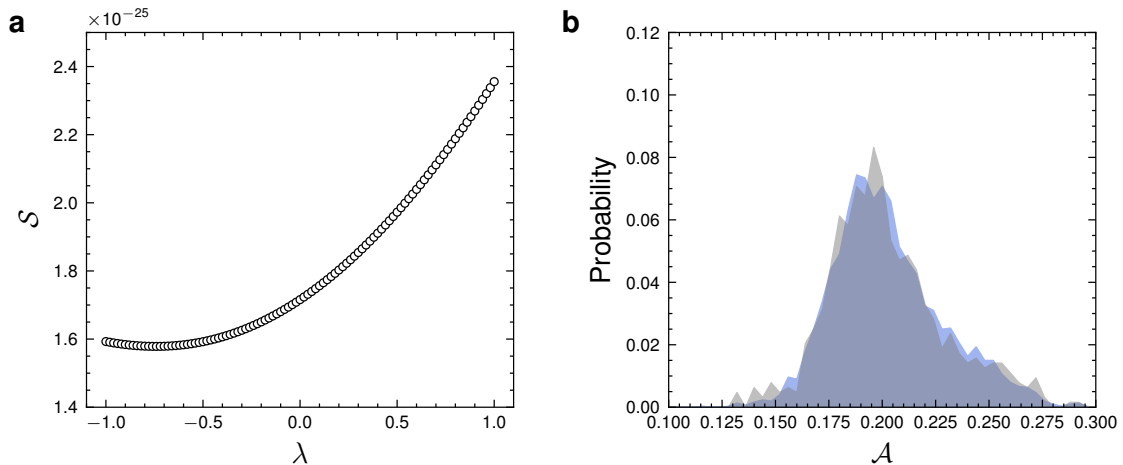


**Fig. S1** (a). The sensitivity as a function of weighted coefficient  $\lambda$  for the force sensing experiment. (b). The anomaly distribution of training (blue) and testing data (gray) of the signal-free experimental outcomes.

where the pixel number  $n_x = 64 \times 64$ . And we analyze the *discrimination loss* (DL) by computing the distance of the feature layer between real and fake image

$$\mathcal{A}_D(\mathbf{x}) = \frac{1}{n_f} \sum |h(\mathbf{x}) - h(G^*(E^*(\mathbf{x})))|, \quad (\text{S9})$$

where we choose the last layer of *discriminator* (before the last activation layer) which is an one-dimensional array with size  $8 \times 8$  as the feature layer  $h(\cdot)$ . We also discuss the important effect from the weighted coefficient  $\lambda$  in the definition of anomaly score (Eq. (2)). Without loss of generality, we use the optimal lambda  $\lambda_{\text{op}}$  to realize the maximum sensitivity  $\text{argmax}_{\lambda \in [-1, 1]} \mathcal{S}(\lambda)$ . In Fig.S1.(a-b), we present the sensitivity as a function of  $\lambda$  for the force sensing experiment. We thus choose the  $\lambda_{\text{op}} = -0.76$  to calculate the anomaly score for inputting atomic images. In addition, we testify the generality of our trained model by calculating the anomaly score for the testing data which is not included in the training dataset. We compare the anomaly distribution of testing and training datasets in Fig. S1, which showing the high universality of method in our setups.

### S-3 The survey on the digital replica

In this section, we present the statistic result of survey on the digital replica. Firstly, we randomly sample data from real datasets to generate a group containing 64 real TOF atomic images. Secondly, we form a mixture of real data and fake data with a probability 50%:50%. We randomly select 30 Ph.D. students and let them know how these groups are formed. They are asked to identify which ones of the second group are real experimental data. We present the statistic result in Fig. S2, where the averaged accuracy is 48(9)% with one-sigma uncertainty.

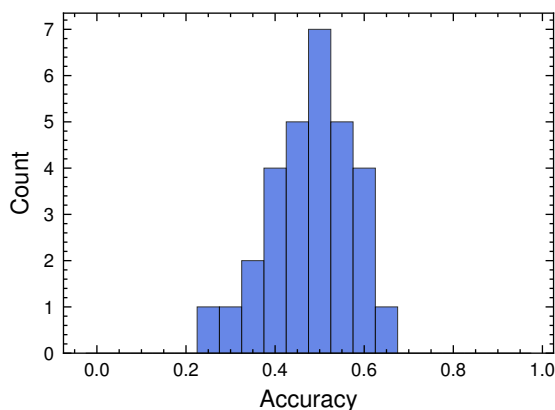


**Fig. S2** The histogram of count number as a function of accuracy for the survey on 30 Ph.D. students.

## S-4 Feature discrimination by t-distributed stochastic neighbor embedding (t-SNE).

The *t-distributed stochastic neighbor embedding* (t-SNE)[45] is a widespread tool in data analysis. It is a nonlinear dimensionality reduction technique by embedding high-dimensional data into a low-dimensional space (two or three dimensions). Specifically, a  $N$ -dimension scalar  $\mathbf{x}$  can be embedded into a dot in the two-dimension t-SNE space. Remarkably, the similarity between two objects  $\{\mathbf{x}^i, \mathbf{x}^j\}$  are modelled by the Euclidean distance between corresponding dots in a two-dimension t-SNE grid. For a detailed review of the t-SNE technique, we refer to the reference [45]. In our case, we use t-SNE to visualize the similarity between force-free and force-involved feature maps. First, we produce the feature map of datasets  $X$  and  $\tilde{X}$  from the last layer of *discriminator*, e.g.,  $m(\mathbf{x}) = h(D^*(E^*(\mathbf{x})))$  which is a  $8 \times 8$  tuple, where the pixel-wise  $m[i, j] \in [0, 1]$ . According to the anomaly score Eq.(2), the DL  $\mathcal{A}_{\mathcal{D}}$  is characterized by feature deviation, and it plays an important role in improving the digital replica in our case (see the discussion on the weighted coefficient  $\lambda$ ). To visualize how the feature map reflects the efficiency of GAN, we next use the t-SNE to embed the 64-dimension feature layer into a two-dimension space. In Fig.S3, we display the feature map of real images for force-free (blue dots) and force-involved (red dots) data in two-dimension t-SNE space. The distinct clusters indicate that our model captures unique features resulting from signal interaction, highlighting the differences in feature deviations between the presence and absence of force. This demonstrates the ability of our GAN model to effectively capture normal variability in signal-free datasets, and it has capacity to detect weaker signal respond.

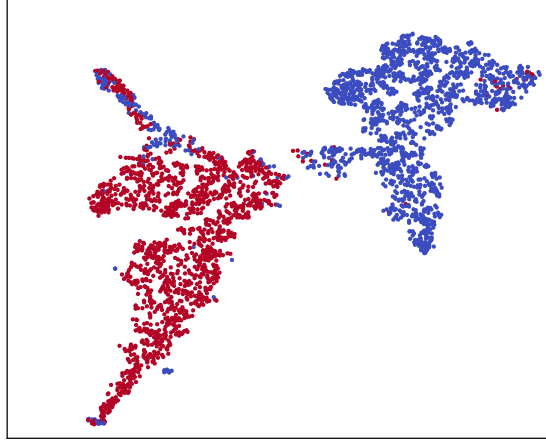


**Fig. S3** The feature layer can be reduced in 2D t-SNE space, where the force-free  $h(x)$  and force-involved  $h(\tilde{x})$  are represented by blue and red dots.

## S-5 Noise reduction by Gaussian process

**The Gaussian Process.** First, we use the Gaussian-Based convolution method to reduce the pixel noise of atomic images. A Gaussian filter, also known as a Gaussian smoothing filter or Gaussian blur, is a commonly used image processing technique for reducing image noise, where an isotropic Gaussian filter is defined as  $g(i, j) = \frac{1}{\sqrt{2\pi}\sigma} e^{-\frac{i^2+j^2}{2\sigma^2}}$  with standard deviation  $\sigma$  in the pixel basis  $i, j = 1, 2, \dots, m$ . The convolution operation involves sliding the kernel over each pixel in the image and computing a weighted average of the pixel values and their neighbors. Mathematically, the convolution operation at each pixel  $\mathbf{x}(i, j)$  can be expressed as follows:  $\mathbf{x}_G(i, j) = \sum[\mathbf{x}(i, j) * g(i, j)]/m^2$ . Here,  $\mathbf{x}(i, j)$  represents the pixel values of the input image,  $g(i, j)$  represents the corresponding values in the Gaussian kernel, and the summation is performed over the kernel's dimensions  $m \times m$ . The size  $m$  determines the dimensions of the kernel matrix, and the standard deviation  $\sigma$  controls the spread of the Gaussian distribution. A larger standard deviation results in a wider distribution, leading to a stronger smoothing effect. Second, we determine the centroid position of absorption images by a Gaussian surface-fitting routine which is widely used in the calibration of the absorption imaging [20, 23, 46]. The two-dimensional elliptical Gaussian function is expressed as

$$G(i, j) = Ae^{-[a(i-i_0)^2+b(i-i_0)(j-j_0)+c(j-j_0)^2]}, \quad (\text{S10})$$

where the amplitude  $A$ , the peak location  $(i_0, j_0)$  and  $a, b, c$  are parameters to be confirmed. The goal is to find parameters  $g = \{A, i_0, j_0, a, b, c\}$  that minimizing the mean-square distance between the Gaussian function  $G(i, j)$  and an atomic image  $\mathbf{x} \in X$ , e.g.,  $\min_{g \in \mathbb{R}} |G(i, j) - \mathbf{x}|^2$ , in the pixel-wise grid  $[i, j]$  where  $i, j = 1, 2, \dots, 64$ . To this end, our Gaussian process upon a probed image can be formulated as  $\mathbf{x}_G = f_G(f_g(\mathbf{x}))$ , where  $f_g(\cdot)$  and  $f_G(\cdot)$  represent Gaussian smoothing and Gaussian-fitting channel, respectively.

Next, we process every raw observable in datasets  $\{X, \tilde{X}\}$  by Gaussian process and compute the corresponding COM. Here, for the sake of simplicity, we use the machine learning toolkit `scipy` to realize the Gaussian fitting process. As a result, we measure the sensitivity  $\mathcal{S}_r^{\text{COM}} = 1.6(5) \times 10^{-24} \text{ N}/\sqrt{\text{Hz}}$ . This noise reduction process benefits the sensitivity compared with the result with raw data  $\mathcal{S}^{\text{COM}}$ . Meanwhile, the data preprocessing may erase valuable information contained in the raw data, implying a lower signal sensitivity compared with our method  $\mathcal{S}^{\text{AS}}$ . Balancing the noise reduction and information loss is another critical issue that we leave here for further investigation. Our method relies on no data preprocessing but offers a more sensitive signal than the conventional configuration with data analysis.

## S-6 Training Saturation

The data burden is the core problem in machine learning applications. Despite the fact that unsupervised learning requires much less than the supervised learning counterpart, it is crucial to balance the experimental cost and resulted accuracy.

This section aims to explore the optimal number of experiment counts to achieve signal detection with acceptable sensitivity. To do so, we randomly sample  $N$  data points from the original datasets and utilize this dataset to train our generative model, employing the same methodology described in the main context’s Method section. Subsequently, we use the corresponding fixed model to generate the anomaly score for the original dataset consisting of  $3.6 \times 10^3$  data points. In Fig.S4, we present the sensitivity as a function of training amount  $N$ , where each data point with one-sigma uncertainty over ten training experiments. For comparison, we establish a sensitivity threshold which is  $\mathcal{S}_c = 6.7 \times 10^{-25} \text{ N}/\sqrt{\text{Hz}}$ . This threshold is calculated when the signal change is equivalent to the one-sigma uncertainty of the health distribution ( $\delta q = \sigma_0$ ). Sensitivities below this critical value are considered indicative of unreliable signal detection. The figure shows that the sensitivity reaches the reliable regime when the training size exceeds one hundred. It is important to note that, for comparison, results in Fig.S4 employ the same optimizer and identical neural network structures for the GAN training process. However, they differ in learning rate and batch size to ensure the confident results. This training saturation is important to estimate the experiment cost of preparing training datasets for our method. It implies that the data acquisition for our method only requiring tens of hours.

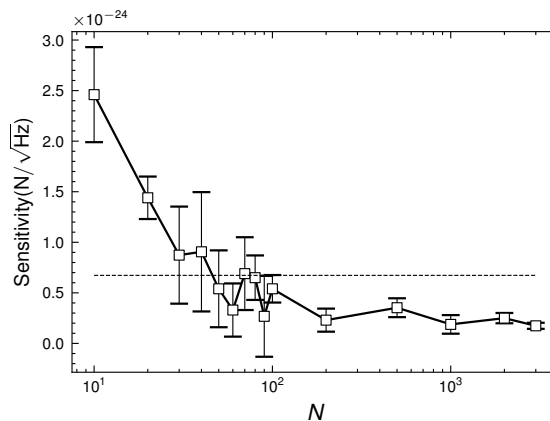


**Fig. S4** The sensitivity of force sensing versus different amount of training data based on the anomaly detection method. The error bar denotes the one-sigma uncertainty over ten training outcomes. The dashed line refers to the critical sensitivity  $6.7 \times 10^{-25} \text{ N}/\sqrt{\text{Hz}}$ .